JOURNAL OF GEOPHYSICAL RESEARCH, VOL. 101, NO. C8, PAGES 18,315–18,326, AUGUST 15, 1996

On the mesoscale interaction of lead ice and floes

Mark A. Hopkins

U.S. Army Corps of Engineers, Cold Regions Research and Engineering Laboratory, Hanover, New Hampshire

Abstract. The plasticity of the Arctic ice pack depends on its granular nature, in particular on the size and distribution of areas of thin ice and open water surrounding multiyear ice floes. The paper begins with construction of a mesoscale (10–100 km) granular model of the central Arctic ice pack. The mesoscale model is based on a dynamic particle simulation in which individual multiyear ice floes and surrounding parcels of first-year ice are explicitly modeled as discrete, convex polygons in a two-dimensional domain. Deformation of the domain produces areas of localized failure and areas of open water. The areas of localized failure are modeled as pressure ridging events using the results of numerical experiments performed with a computer simulation of the ridging process. The paper focuses on the results of numerical experiments performed with the mesoscale model. In the experiments the model ice pack is biaxially deformed at constant strain rates. The principal strain rates are varied to create deformation states ranging from pure shear to uniform compression. The results define the shape and magnitude of the plastic yield surface, the strain rate vectors associated with points on the yield surface, the partition of energy dissipation between ridging and in-plane sliding, and the changes in the ice thickness distribution associated with various deformation states.

Introduction

The Arctic Ocean is covered by a permanent ice pack. Large-scale sea ice models of the Arctic ice pack [*Hibler*, 1979] typically relate the strength of the ice pack to the ice thickness using a plastic rheology. The plasticity of the Arctic ice pack intrinsically depends on its granular nature, in particular on the size and distribution of areas of thin first-year ice and open water surrounding thick multiyear floes. Deformation of the ice pack causes relative motion between floes, which in turn causes the thin ice to fail irreversibly. The rubble created in the process is piled up and down to form the pressure ridges that crisscross the pack. Sea ice models [*Hibler*, 1979], which treat the ice pack as a continuum, incorporate plasticity by assuming the shape of the plastic yield surface, the flow rule associating stresses and strains, and a complex relationship between ice strength and the ice thickness distribution. There is, at present, little empirical knowledge on which to base these assumptions.

With the computer power currently available, it has become possible to explicitly model granular processes in great detail using particle simulations. A particle simulation is a computer program that models the dynamics of a system consisting of a large number of interacting particles such as, in this context, ice parcels. While it is not yet possible, or perhaps even desirable, to model the entire Arctic Basin, it is possible to model, in considerable detail, a section of the ice pack of several hundred square kilometers containing several thousand parcels.

This paper begins with the development of a dynamic, mesoscale (10–100 km) numerical model of the central Arctic ice pack. The model embodies the granularity of the ice pack by explicitly considering individual multiyear floes in a matrix of first-year ice parcels. The individual ice parcels are irregularly shaped, convex polygons in a two-dimensional domain. The results of early work with this model, using a single thickness of first-year ice, are described by *Hopkins* [1993]. In the present work, thicknesses are assigned to each parcel according to an assumed ice thickness distribution. Biaxial deformation of the domain creates relative motion between neighboring parcels of ice. Since the polygonal parcels initially fill the domain, relative motion causes some parcels to overlap. At each site where overlap occurs, the overlapping portion of the thinner ice parcel is assumed to have failed, forming a pressure ridge along the line of contact. A force, resisting further convergence, is calculated and applied at each site on the basis of the amount of ridged ice at the site. The parametrization of the ridging force, the force required to enlarge a pressure ridge, in terms of the amount of ridged ice is based on the results of numerical experiments performed with a computer simulation of the ridging process [*Hopkins*, 1994].

The focus of the paper is on numerical experiments performed with the mesoscale model. In the experiments the model ice pack is biaxially deformed at constant strain rates. The principal strain rates are varied to create deformation states ranging from pure shear to uniform compression. Three major topics are addressed in the experiments.

1. The stresses created in the domain in the various deformation states by the mechanism described above define a yield surface in principal stress space. The sensitivity of the shape and magnitude of the yield surface to the friction coefficient between ice parcels and prior deformation of the ice pack is explored. The strain rate vectors associated with points on the yield curves are also shown.

2. Energy is dissipated during deformation by pressure ridging and by in-plane, frictional sliding between ice parcels. The partition of energy dissipation between ridging and sliding is determined through the explicit calculation of the energy dissipated at each contact.

3. The changes to the ice thickness distribution in the model ice pack are calculated by adding the changes at each ridging site. Since only two-dimensional, in-plane deformation

Paper number 96JC01689.

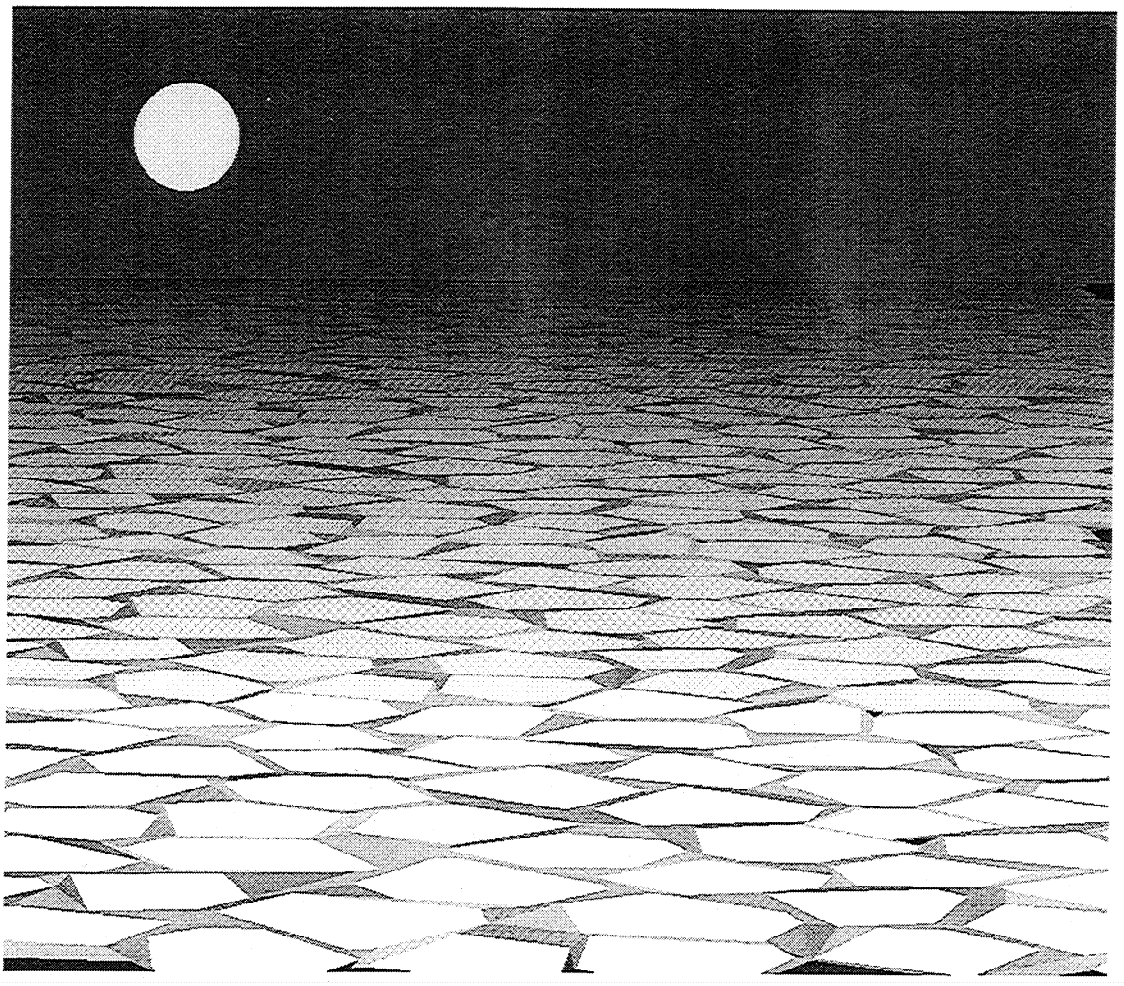

Figure 1. Perspective drawing of the model ice pack. The periodicity of the pack is evident in the repetition of features.

is explicitly modeled, this calculation is based on an average ridge profile, that is, a function of the volume of ridged ice, obtained from pressure ridging simulations [*Hopkins*, 1996].

Mesoscale Ice Pack Model

The mesoscale ice pack model is based on a particle simulation, in which a computer program is used to model the dynamics of a system consisting of a large number of discrete ice parcels. The shape, position, orientation, and velocity of each parcel are stored in arrays. At each time step the contact and body forces on each parcel are calculated, and the parcels are moved to new locations with new velocities that depend on the current forces.

The model ice pack, shown in Figure 1, is composed of convex polygonal parcels of ice capable solely of in-plane motion. The thicknesses of the parcels are chosen according to an assumed ice thickness distribution. Interaction between parcels begins with elastic loading followed by plastic failure. Plastic failure occurs through crushing, if the thickness of both parcels is greater than a critical thickness h^*, or as pressure ridging, if the thickness of one parcel is less than h^*. The term "crushing" in this work refers to the pressure-driven granulation that occurs when two thick ice sheets are pushed together. The term "pressure ridging," on the other hand, refers to the flexural failure of an ice sheet and subsequent piling of the ice blocks created by the flexural failure on top of and beneath the opposing ice sheet. In-plane ridging forces are based on the results of pressure ridging simulations [*Hopkins*, 1994]. Relative tangential motion between parcels in contact gives rise to in-plane frictional forces. A description of the important features of the ice pack model follows. A description of the general mechanical details of the particle simulation technique is provided by *Hopkins* [1992].

The domain of the simulation is a square, periodic control area. The model ice pack fills the domain. In Figure 1, which is composed of multiple images of the model pack, periodic features are evident. The domain is periodic in that an ice parcel that leaves the domain through one boundary simultaneously reenters the domain through the opposite boundary. Opposing boundaries are connected in the sense that parcels on one boundary interact with parcels on the opposite boundary. Deformation of the domain is accomplished by distorting the domain by specifying the principal strain rates which are held constant for the duration of each simulation. Although the mean motion of the ice parcels is constrained, their velocities fluctuate in response to contact forces. This simulation technique using a periodic domain was developed by *Cundall and Strack* [1979] to create a mean deformation field in a granular material without the use of solid boundaries that cause inhomogeneities. This technique was used by *Hopkins and Hibler*

[1991] in earlier simulations of the ice pack using disk-shaped ice floes. It should be emphasized that the average of the instantaneous strains measured between pairs of parcels at any time during a simulation must equal the imposed strain rate.

The model ice pack is composed of polygonal parcels of thick multiyear ice and thinner first-year ice. The construction of the model ice pack begins with a Voronoi diagram [*Fortune*, 1987] of a square domain. The edge polygons in the diagram are discarded. The remaining polygons are the multiyear ice parcels or floes. The domain is dilated, while the size of the floes is held constant, to separate the floes. The floes are given a random velocity and allowed to move around, freely colliding, until their initial orderly arrangement is completely lost. The domain is then compressed to bring the fractional area covered by multiyear ice to the desired value. The interstitial area among the floes is filled with convex polygonal parcels of thin ice. The thin ice parcels and shaded floes that compose the model ice pack are shown in Figure 2. The thicknesses of the ice parcels are randomly assigned according to an assumed ice thickness distribution.

Since the polygonal ice parcels initially fill the domain, compression of the domain causes the parcels to overlap or intersect. The force between a pair of intersecting parcels is based on the area of intersection and acts at the centroid of the area. An elastic-viscous-plastic normal force model is used with a Mohr-Coulomb tangential force model. The elastic component provides the elastic loading that precedes and accompanies plastic failure. The viscous component dampens elastic waves. The plastic component models crushing failure in ice thicker than h^* and pressure ridging in ice thinner than h^*. Tensile forces are not considered. A typical contact between a parcel of thin ice and a floe is shown in Figure 3. The line of contact AB between the two parcels is defined by the intersection points of their perimeters. A local coordinate frame n, t is defined by the normal n perpendicular to the line of contact. The area of overlap shown in the figure is considered to be

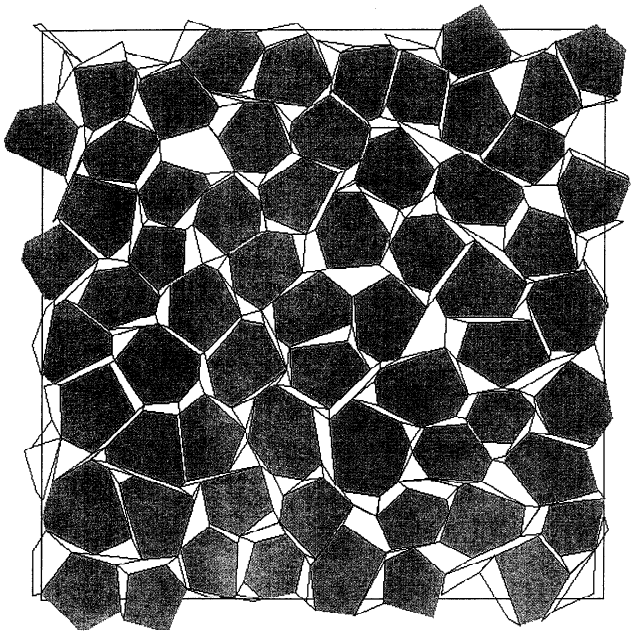

Figure 2. Square domain area containing the polygonal ice parcels. The gray polygons are thick floes, and the white polygons are parcels of thin ice.

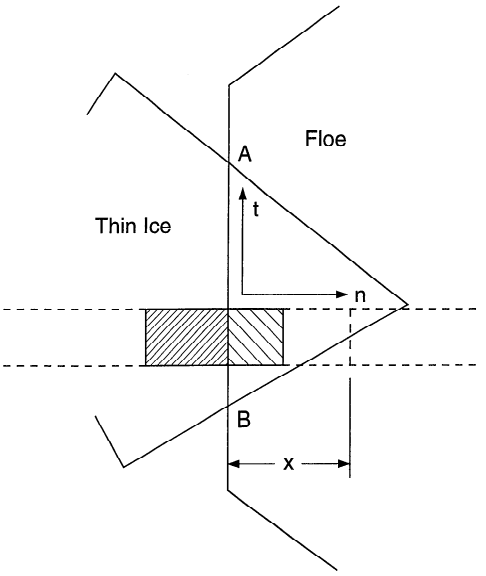

Figure 3. Typical contact between a parcel of thin ice and a floe. The line AB is the line of contact. The length x is the average intrusion of the strip of thin ice denoted by the dashed lines across the line of contact AB. The shaded parts of the strip correspond to the ridge cross section shown in Figure 4.

ridged ice broken from the thin ice sheet. The pair of horizontal dashed lines that cross the thin ice and floe polygons in Figure 3 define a strip of unit width. A cross section of a ridge corresponding to the strip in Figure 3 is shown in Figure 4. The diagonally shaded areas of the strip in Figure 3 correspond to similarly shaded areas of the sheet and floe covered by the ridge cross section in Figure 4.

The parametrization of ridging forces is based on the results of simulations performed with a computer model of the pressure ridging process [*Hopkins*, 1994]. This model was based on the assumption that ridges are created by a thin sheet impacting a thick floe. The thin sheet was assumed to fail in flexure. The ridge building force (in newtons per meter of ridge length, the direction perpendicular to the page in Figure 4) determined from the simulations was

$$F = h(928V + 26{,}126) \tag{1}$$

in which h is the thickness in meters and V is the volume of ridged ice in meters cubed per meter of ridge length. The length x in Figure 3 refers to the average intrusion of the strip of thin ice across the line of contact AB. The volume of ridged

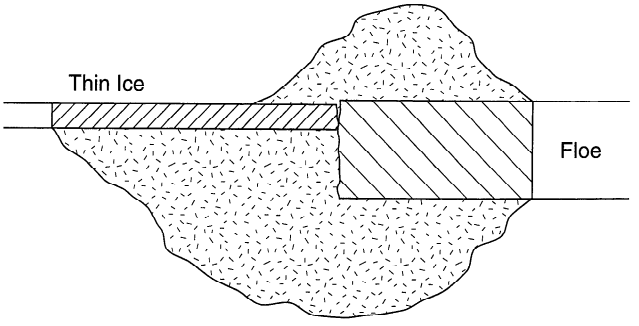

Figure 4. Ridge cross section corresponding to the shaded strip in Figure 3, showing the ridge sail and keel.

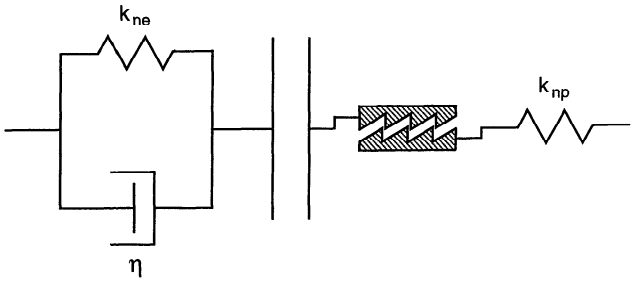

Figure 5. Normal direction contact force model.

ice in the strip is hx, the product of ice thickness and the length x of the strip. Equation (1) has a linear component that increases with V and a constant component proportional to the strip width. Elastic loading of the floe and thin ice accompanies the increase in the ridge building force. A diagram of the force model used to calculate the compressive force between the two ice parcels in the strip is shown in Figure 5. The coefficient k_{ne} is the elastic contact stiffness, and η is the viscosity coefficient. The ratcheting slider in Figure 5 is used to model nonrecoverable plastic deformation due to pressure ridging or crushing. Pressure across the slider imposes a contant drag k_r on the contact in the direction of loading. If the contact is ridging, then $k_r = 26126h$ N/m from (1), and if the contact is crushing, then $k_r = h\sigma_c$, the ice compressive strength. The stiffness coefficient k_{np}, used to model "plastic hardening," is the value $928h^2$ N/m^2 from (1) if the contact is ridging but is set to zero if the contact is crushing.

The mechanism shown in Figure 5 permits two types of deformation. If the force is sufficient to move the ratcheting slider (ridge growth or crushing), then elastic loading is accompanied by plastic deformation; otherwise, only elastic loading occurs. The two types of deformation require separate equations. The first equation

$$F = k_{ne}x_e + \eta\dot{x}_e \tag{2}$$

applies in the absence of plastic deformation. The overdot denotes the time derivative. The elastic deformation x_e is measured across the spring and dashpot. The second equation

$$\dot{x} + (k_{ne}/\eta)x = (1/k_{np})\dot{F} + (1/\eta)[1 + (k_{ne}/k_{np})]F - (1/\eta) \cdot (k_{ne}/k_{np})k_r \tag{3}$$

applies when plastic deformation accompanies elastic loading. The variable x is the total deformation across the spring and dashpot and ratcheting slider. It is assumed that the entire contact is undergoing one type of deformation or the other. With this assumption both (2) and (3) can be integrated along the entire line of contact in Figure 3 to obtain analogous expressions for the normal force in the two regimes,

$$F_n = k_{ne}A_e + \eta\dot{A}_e \tag{4}$$

$$\dot{A} + (k_{ne}/\eta)A = (1/k_{np})\dot{F}_n + (1/\eta)[1 + (k_{ne}/k_{np})]F_n - (1/\eta)(k_{ne}/k_{np})Wk_r \tag{5}$$

where W is the length of the contact surface, A is the total overlap area in Figure 3, A_e is the elastically deformed part of the total area, and the subscript n on F denotes the normal component of the contact force. The assumption that the entire contact is in one regime implies that differential motion along the line of contact, caused by relative rotation of the two parcels, is ignored. Equations (4) and (5) are solved separately for the normal force F_n using backward difference approximations for the derivatives. The lesser of the two values is used.

A representation of the tangential contact force model is shown in Figure 6. The tangential force F_t increases because of slip between the polygons at the contact surface in the tangential direction. Initial relative motion between the polygons, which increases the tangential force by compressing the spring in the figure, simulates elastic loading of the material. The tangential force is not allowed to exceed the Coulomb limit μF_n. At that point the ice parcels begin to slip relative to one another. The equations defining the tangential force are

$$\dot{F}_t = -Wk_{te}V_{(1/2)t} \tag{6}$$

$$|F_t| \leq |\mu F_n| \tag{7}$$

where the overdot denotes the time derivative, k_{te} is the tangential elastic stiffness, and $V_{(1/2)t}$ is the tangential component of the relative velocity at the point of contact. The tangential stiffness k_{te} is found from the normal stiffness and Poisson's ratio ν by analogy to the shear modulus and Young's modulus using the expression $k_{te} = k_{ne}/2(1 - \nu)$. Some viscosity is used in parallel with the elastic force for stability.

The calculation of the effective contact stiffness k_{ne} is a problem in its own right. In granular flow simulations, a constant linear spring stiffness or a Hertzian model is typical. At the other extreme, one might use a concurrent finite element calculation to determine the effective stiffness of each contact between ice parcels. In this work a crude effective contact stiffness for each ice parcel is calculated. The majority of contacts in the model ice pack consist of rather long, slender parcels of thin ice compressed between floes as shown in Figure 2. When a rectangular parcel is loaded along its long sides, the stiffness per unit length is

$$k_{ne} = Eh/L \tag{8}$$

where E is the elastic modulus and L is the width of the parcel. This estimate is extended to irregular shapes by adopting an effective L

$$L = A/(2\langle R\rangle) \tag{9}$$

where A is the polygon area and $\langle R\rangle$ is the average of the distances from the center of mass to each vertex. Contacts

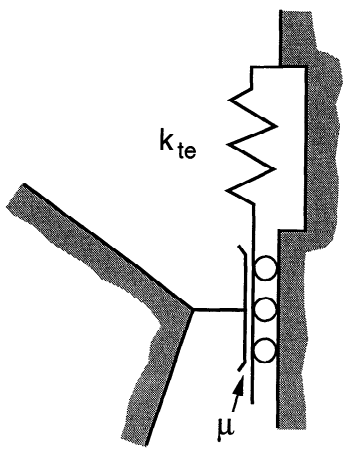

Figure 6. Tangential direction contact force model.

between pairs of floes typically consist of point loadings. The effective stiffness of floes in contacts involving point loads is underestimated by the approach outlined above. Therefore a large, constant value of the stiffness coefficient k_{ne} is used for the floe parcels. The effective stiffness coefficient in a contact between two parcels is a series combination of the coefficients for each parcel

$$1/k_{\text{eff}} = 1/k_1 + 1/k_2 \tag{10}$$

The effective viscosity coefficient is calculated in the same way. The water drag on each ice parcel is found from a simple quadratic relationship

$$F_w = -c_w \rho_w A u_i |u_i| \tag{11}$$

where ρ_w is the water density and u_i is the parcel's velocity. The parcel velocity u_i is a fluctuating velocity with respect to the mean motion $e_{ij}x_j$ at its center of mass.

After the contact and body forces exerted on each parcel have been found, the equations of motion are solved for new positions and velocities and time advanced one step. The equations that define ice motion are standard difference equations derived from a Taylor series expansion about the current time. At each time step Δt, the change in the position of each parcel has a component due to the velocity of the parcel and to the simultaneous deformation of space:

$$x_i^{n+1} = x_i^n + \Delta t(u_i^{n+1/2} + e_{ij}x_j^n) \tag{12}$$

where the superscript n denotes the time step, the subscripts i and j denote directions in Cartesian space, and e_{ij} is the uniform strain rate imposed on the domain. The parcel's fluctuating velocity at time $n + 1/2$, which changes in response to contact and body forces on the parcel i at time n, is

$$u_i^{n+1/2} = u_i^{n-1/2} + \Delta t F_i^n / m_i \tag{13}$$

where F_i is the resultant of the contact forces on the ice parcel and m_i is its mass. The strain rate enters the velocity calculations only when computing the relative velocity between two ice parcels.

Rotational motion is computed using similar equations. At each time step the orientation of parcel i is

$$\theta_i^{n+1} = \theta_i^n + \Delta t \omega_i^{n+1/2} \tag{14}$$

The rotational velocity ω_i of parcel i at time $n + 1/2$, which changes in response to the torque T_i caused by contact and body forces on the parcel, is

$$\omega_i^{n+1/2} = \omega_i^{n-1/2} + \Delta t T_i^n / I_i \tag{15}$$

where I_i is the polar moment of inertia of the ice parcel.

Energetics

The work performed to compress the ice pack is the double dot product, $\sigma_{ij}e_{ij}$, of the stress tensor σ and the strain rate tensor e integrated over the duration of an experiment. The stress tensor σ_{ij} is calculated using the equation [*Cundall and Strack*, 1979]

$$\sigma_{ij} = [\Delta t/(TA)] \sum r_i F_j \tag{16}$$

where r_i is the vector connecting the center of two polygons, F_j is the force between them, T is the experiment duration, and A is the area of the model domain. The summation is over every contact at each time step.

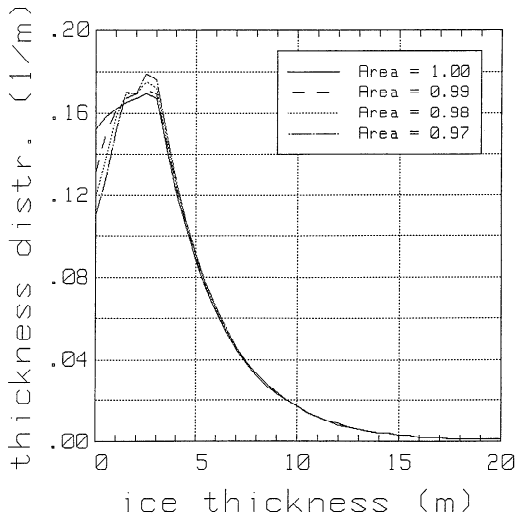

Figure 7. Ice thickness distribution. The solid line denotes the initial distribution. The dashed, dotted, and dash-dotted lines denote the distribution following 1%, 2%, and 3% uniform convergence, respectively.

The energy lost due to frictional sliding and plastic deformation is found by integrating the work performed at each contact. The frictional dissipation Φ_f, which is the work performed by the tangential contact forces, is

$$\Phi_f = \Delta t \sum F_t V_{(1/2)t} \tag{17}$$

Similarly, the inelastic dissipation Φ_i due to viscosity and ridging, which is the net work performed by the normal contact forces, is

$$\Phi_i = \Delta t \sum F_n V_{(1/2)n} \tag{18}$$

In (17) and (18) the summations are over every contact at each time step. The energy balance calculated from (17) and (18), combined with much smaller amounts lost to water drag and the change in kinetic energy, is compared with the deformational work calculated from (16) as a check on the self-consistency of the simulation. The error in the energy balance was no greater than 1% of the total work performed.

Experiments With the Model Ice Pack

Three samples of the model ice pack were created according to the method described above. The square samples were initially 13.4 km wide. Each sample contained approximately 65 floes and 268 first-year ice parcels. The average floe size was 2.06 km^2 with a standard deviation of 0.33 km^2. The sample ice packs contained 75% multiyear ice by area. The first-year ice thicknesses were assigned according to the initial distribution shown in Figure 7. The distribution is taken from *Wadhams* [1981], with some ice added to the thin end and subtracted from the thick end. The mean ice thickness of the initial distribution is 3.8 m. The distribution decreases exponentially for thicknesses greater than 3 m. The parcels were chosen at random and assigned thicknesses beginning at the thin end of the distribution. The thickest first-year parcel was about 1.6 m thick. The remainder of the thickness distribution was distributed over the floes.

Table 1. Parameters Used in the Experiments

Parameter	Symbol	Value
Strain rate invariant	e	2×10^{-6} s^{-1}
Experiment duration		500 s
Floe elastic stiffness	k_{ne}	50 MN m^{-2}
Ice compressive strength	σ_c	2.6 MPa
Elastic modulus of first-year ice	E	1 and 3 GPa
Maximum ridging thickness	h^*	1.25, 1.375, and 1.5 m
Friction coefficient	μ	0.2, 0.5, and 0.8
Seawater density	ρ_w	1010 kg m^{-3}
Ice density	ρ_i	920 kg m^{-3}
Poisson's ratio	ν	0.33
Water drag coefficient	c_w	0.005

Each sample was uniformly compressed in three stages, reducing the area to 99%, 98%, and 97% of the initial area. (In the following discussion and in the accompanying figures, the results of experiments performed with each sample are referred to by the area of the sample used in the experiment, for example, area = 99%). Compressing the samples has the twofold effect of reducing the areas of unridged thin ice and increasing the amount of ridged ice at each ridging site. Figure 7 shows the effect of compressing the samples on the ice thickness distribution.

Each of the three samples, at each of the three stages of compression, was deformed using a range of strain fields from pure convergence to pure shear. The strain fields were created by varying the principal strain rates e_1 and e_2 such that the strain rate invariant

$$e = 2^{1/2}(e_1^2 + e_2^2)^{1/2} \tag{19}$$

was held constant. The value of the strain rate invariant, as well as other parameters used in the experiments, is given in Table 1. The strain rate invariant used in the simulations is greater than typical values from the literature in the interest of computational efficiency. Inertial effects due to the high strain rate were insignificant. Values of ρ_w, ρ_i, and c_w used in the simulations were taken from *Hibler* [1986]. Values of E, ν, and σ_c were taken from *Mellor* [1986]. The floe elastic stiffness k_{ne} was chosen to be sufficiently large that it would not affect the results. The friction coefficient μ, governing sliding contacts between ice parcels, is unknown. A range of values were examined.

Each test was begun in a relaxed state. All ice motion was arrested, and any residual elastic deformation was removed. A uniform strain field was applied to a sample, and the stress state in the sample was continuously monitored. Figure 8 shows the increase in the principal stresses σ_1 and σ_2 as a function of strain measured from the onset of deformation. Strain is calculated as the product of time and the strain rate invariant (equation (19)). The top pair of lines corresponds to a state of uniform convergence, while the bottom pair corresponds to a state of pure shear. Initially, the stress level rises quickly as the elastic loading at each contact increases. The rate of increase depends on the elastic modulus of the thin ice. After rising rapidly, the rate of increase levels off. For the yield curves which follow, stress levels were estimated by averaging the stresses over the final 20% of strain.

The assumption of a critical ice thickness h^* creates two modes of plastic failure for the interactions between neighboring ice parcels. One, ridging of thin ice, caps elastic forces at low levels, and the other, crushing of thick ice, caps elastic forces at very high levels. The existence of the two failure modes implies a critical concentration. The critical concentration is reached when the area of undeformed thin ice ($h < h^*$) decreases to the point where the loading paths that cross the model pack no longer contain thin ice. As concentration approaches the critical point, the stress levels rise steeply with further strain. The experiments discussed here were performed at concentrations below the critical concentration defined by a rapid rise in the stresses with continued strain.

The parameter h^* is used in lieu of a more complete understanding of the ridging process. In simulations using a computer model of the ridging process [*Hopkins*, 1994], ridges were formed from an intact sheet of thin ice pushed against a thick floe. The blocks composing the ridge sail and keel were broken from the thin sheet in flexure. At the other extreme, where two thick sheets or floes are driven together, it is hard to imagine anything but crushing taking place. The critical thickness h^* is used to define a point of transition between ridge growth based on predominantly flexural failure and failure predominantly by crushing. In reality, the transition from a purely ridging to a purely crushing failure mode probably takes place gradually over a wide range of ice thickness.

The effect of sample size was examined by creating three larger (17.2 km wide) and three smaller (8.8 km wide) square samples of the model pack. Experiments were performed with the samples using the same average floe size, thickness distribution, and other parameters used in the experiments with the 13.4-km-wide model pack. A comparison of the results of the three sets of experiments showed no size effects.

Stresses and Yield Curves

A plastic yield curve is a plot in stress space showing the state of stress in a material undergoing plastic failure. Ice-ocean models of the Arctic Basin [*Hibler*, 1979; *Flato and Hibler*, 1995] use an assumed elliptical yield curve to characterize the internal strength of the pack. A state of stress on the yield curve is associated with a strain rate vector using the normal flow rule. A family of curves, obtained from experi-

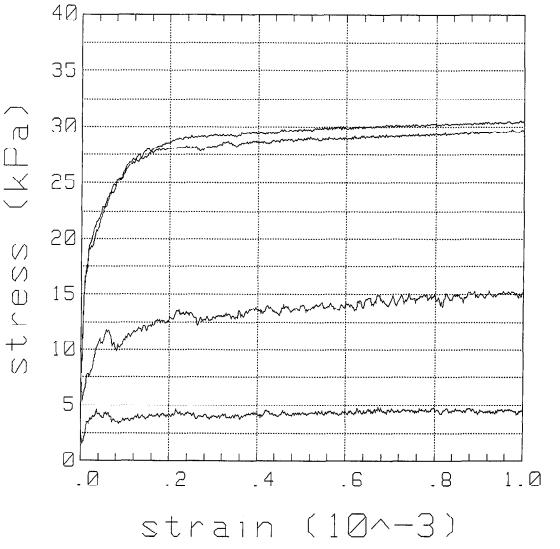

Figure 8. Principal stresses as a function of strain. The top pair of lines is from a uniformly convergent strain field, while the bottom pair of lines is from a state of pure shear.

ments with the model pack, is shown in Figure 9. The axes in the plot represent compressive stresses. The curves are partial curves corresponding to deformation fields ranging from one state of pure shear ($e_1 = -e_2$, $e_1 < 0$) through pure compression ($e_1 = e_2$) through the opposite state of pure shear ($e_1 = -e_2$, $e_2 < 0$). Simulations were performed for deformation states beyond pure shear, which result in net divergence. However, stresses dropped rapidly to zero in the absence of confining pressure in the diverging direction. Tensile forces between ice parcels, which might affect this result, are not considered in this study. The rays attached to the largest curve indicate the strain rate vector associated with a given stress state. The magnitude of the yield curve measured along the axis of symmetry is a function of the compressive strength of the ice pack. The breadth of the yield curve measured perpendicular to the axis of symmetry, that is proportional to the difference between the principal stresses, depends on the shear strength of the ice pack.

The four yield curves in Figure 9 correspond to the four states of initial uniform compression, that is, a sample with area = 100% has undergone no initial compression, a sample with area = 99% has undergone 1% initial compression, and so on. Each curve is an average of results obtained from experiments with three samples. The experiments used values of $E = 3$ GPa, $h^* = 1.375$ m, and $\mu = 0.5$. The growth in the yield curve shows the increasing strength of the model pack caused by the increasing amounts of uniform compressive deformation discussed above. The slight asymmetry of the curves (about the line $\sigma_1 = \sigma_2$) reflects the spatial anisotropy of the model pack. The strain rate vectors attached to the 97% curve are normal to the yield curve only at the point corresponding to pure compression. Choosing a state of stress on the yield curve in Figure 9 using the normal flow rule may cause a large error in estimating the stresses, particularly for deformation states having a large shear component. The error would be equal to the difference between the stresses at the point where the strain rate vector is located in Figure 9 and the stresses at the point where the same strain rate vector is perpendicular to the curve.

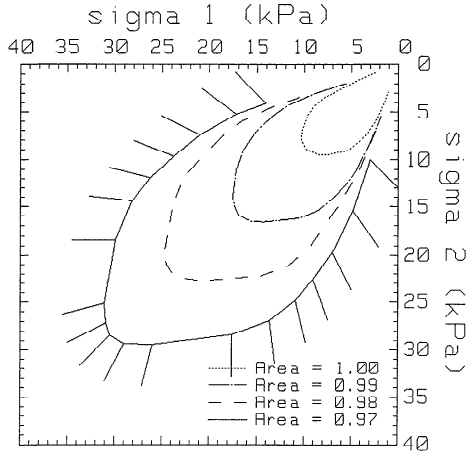

Figure 9. Plastic yield curves in principal stress space for deformation states ranging from pure compression through pure shear. The four curves are obtained from experiments with samples of the model ice pack with area equal to 97%, 98%, 99%, and 100% of the initial area. The short lines attached to the largest curve indicate the strain rate vectors.

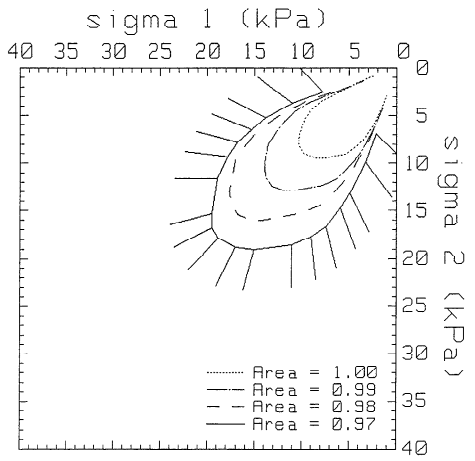

Figure 10. Yield curves obtained by setting the amount of ridged ice at each ridge site to zero in the sample ice packs with area equal to 97%, 98%, and 99% of the initial area.

The growth in the yield curves that accompanies compression, shown in Figure 9, is caused by three factors. The first factor is the change in the ice thickness distribution shown in Figure 7. The reduction in the area of thin ice increases the average thickness of unridged thin ice. The increased thickness increases ridging forces through the thickness term in (1). The second factor is the increase in the amount of ridged ice at each ridge site. Larger ridges increase the ridging forces through the volume term in (1). The third factor might be termed a geometric constraint on deformation. Deformation of the model pack takes place through deformation of the parcels of thin first-year ice. Because of the geometric interrelationships among the multiyear and first-year ice parcels, some parcels of thin ice are more accessible to deformation than other parcels. In deformation, the most accessible parcels of thin ice are the first to be destroyed. Further deformation is forced to follow successively more difficult paths through less accessible parcels of thin ice, resulting in higher stresses. To obtain some idea of the relative importance of the three factors, two sets of comparative experiments were performed.

In the first set of comparative experiments, the ridged ice at each ridge site, which was a result of initial uniform compression of the samples, was removed. The results of the experiments are shown in Figure 10. The four yield curves again correspond to the four states of initial compression. Each curve is an average of results obtained from experiments with three samples. The experiments used values of $E = 3$ GPa, $h^* = 1.375$ m, and $\mu = 0.5$. The results show that the ridged ice was responsible for a large part of the increase in the yield curves in Figure 9.

In the second set of comparative experiments, the initial configuration of the model pack (area = 100%) was initialized with the four ice thickness distributions shown in Figure 7. Thus in the second set of experiments, not only was the ridged ice at each ridge site absent, but since each sample had the same geometry, the effects of increased geometric constraints on deformation were also removed. The four yield curves obtained using the four distributions are shown in Figure 11. The yield curves from the distributions obtained from the compressed samples (area equal to 97%, 98%, and 99% of the initial area) are very close to the yield curve obtained with the initial thickness distribution. The further large reduction in the

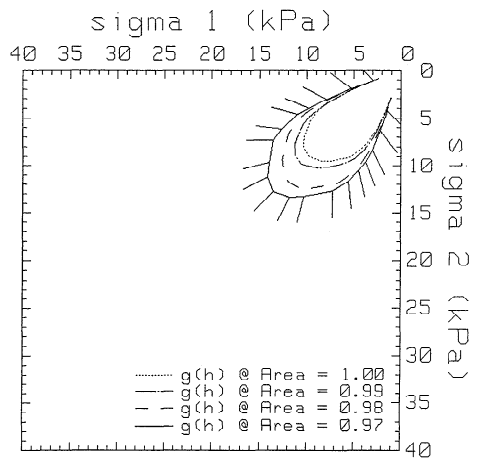

Figure 11. Yield curves obtained using the four ice thickness distributions shown in Figure 7 with the initial configuration.

magnitude of the yield curves demonstrates that the geometric constraints are responsible for a large part of the increase in yield stresses in Figure 9. Furthermore, the small differences among the four yield curves in Figure 11 show that the changes in the thickness distribution have little effect on the yield curves.

Experiments were run to assess the effects of variations of the elastic modulus of the first-year ice. The elastic modulus is related to the contact stiffness by (8). The experiments used values of E of 1 GPa and 3 GPa. The lower value caused the yield curves to shrink by approximately 5%, which is not significant. The value of $E = 3$ GPa was used in all subsequent experiments. Increases in the elastic stiffness of the multiyear ice, beyond the value given in Table 1, had no discernible effect. The experiments used values of $\mu = 0.5$ and $h^* = 1.375$ m.

Experiments were run to assess the effects of variations of the critical thickness h^*. As was mentioned above, ice thicker than h^* fails by crushing. The force required to crush ice is much greater than the force required to induce flexural failure. Thus with the low stress levels in the experiments relative to the crushing strength, reducing the value of h^* has the effect of reducing the area of thin ice available for deformation. The fraction of ice area (in the initial configuration) with thickness less than h^* was 0.17 ($h^* = 1.25$ m), 0.19 (1.375 m), and 0.21 (1.5 m). The magnitude of the yield curves in Figure 12 increases as h^* decreases. The results shown are from experiments using samples with area equal to 97% of the initial area. It is important to note that for the three values of h^*, samples with area of 97% were separately generated by uniformly compressing the initial configuration. The experiments used values of $\mu = 0.5$ and $E = 3$ GPa.

The net deformational area change in an experiment is made up of many small changes at individual ridge sites in the domain. Because of geometric constraints, the ice that is ridged is not necessarily the thinnest available ice. If h^* is reduced, ice parcels with thickness greater than h^*, that previously deformed by ridging, must deform by crushing. Since the stress required to crush ice is so far above the stress levels in the experiments, ice thicker than h^* is practically rigid. This strengthening of a fraction of the first-year ice parcels, by reducing h^*, changes the failure paths throughout the model pack. If, in some total sense, deformation follows the path of least resistance, then any changes that increase the constraints on deformation will also increase stress.

Interestingly, there is an analogous parameter, called G^*, used in thickness distribution theory [*Thorndike et al.*, 1975] to specify the fraction of area available for ridging. Given a thickness distribution, G^* implies a value of h^*. Increasing h^* (by increasing G^*) with a given distribution has the effect of increasing the average thickness of ice being ridged and thereby increasing stresses. Increasing h^* in the present model by decreasing the geometric constraints on deformation produces the contrary effect shown in Figure 12.

Three sets of experiments were run to assess the effects of variations of the friction coefficient μ. The friction coefficient affects the magnitude of the tangential force in sliding contacts between ice parcels. As was explained in conjunction with (6), sliding begins when the magnitude of the tangential force reaches the Coulomb limit. The experiments used values of μ of 0.2, 0.5, and 0.8. The yield curves obtained in experiments using samples with area equal to 97% of the initial area are shown in Figure 13. While reducing μ from 0.8 to 0.5 had a modest effect, further reduction had a much larger effect on the size of the yield curves. Similar changes occurred in samples with area of 98% and 99%. The experiments used values of $E = 3$ GPa and $h^* = 1.375$ m.

The effects of changes to the friction coefficient are nonlinear. The obvious immediate effect of reducing the friction coefficient is to reduce the tangential force that resists motion in sliding contacts. Since the tangential contact forces contribute to the overall stress level, the stress level will decrease as well. A decrease in the overall stress level will, in turn, reduce confining pressures and normal forces at sliding contacts, further reducing the tangential forces. In addition, by facilitating sliding, decreasing the friction coefficient may bring into play otherwise inaccessible areas of thin ice, further reducing stress.

The major and minor principal stresses are calculated from the contact forces between ice parcels using (16). The contact forces have normal and tangential components given by (4)–(7). The contributions to each of the two principal stresses by the normal and tangential components of the contact forces can be separated. The ratio of the tangential to the normal components of the two principal stresses is shown in Figure 14. The abscissa is the ratio of the principal strain rates which

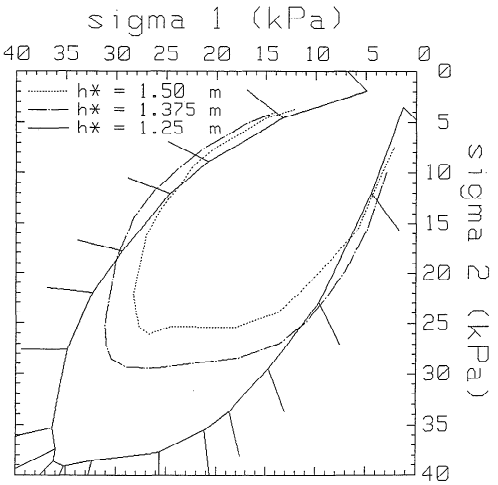

Figure 12. Yield curves obtained using the 97% configurations and various values of the critical ice thickness h^*.

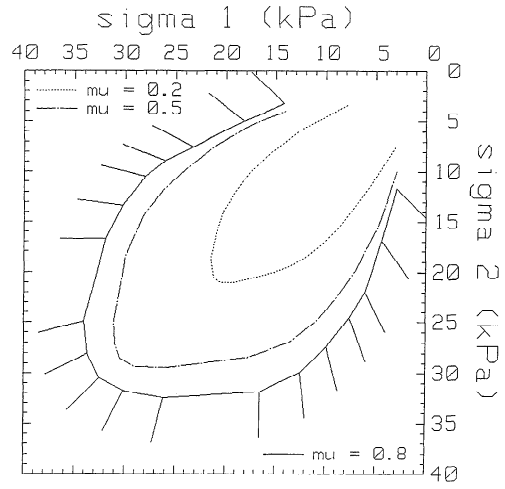

Figure 13. Yield curves obtained using the 97% configurations and various values of the friction coefficient μ.

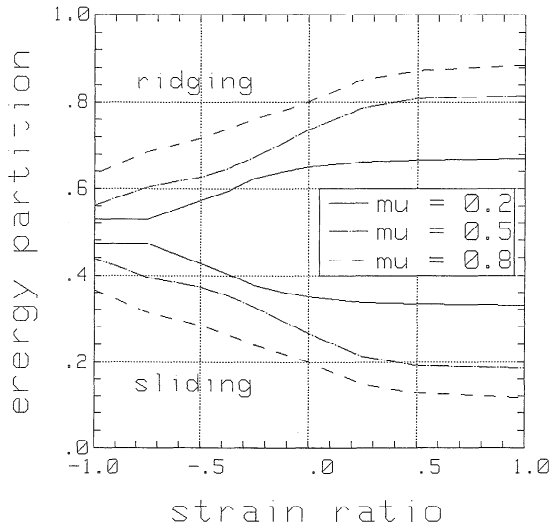

Figure 15. Energy partition between ridging and in-plane sliding modes of local deformation for three values of the friction coefficient μ (using the 97% configurations).

varies from -1 in a state of pure shear to $+1$ in a state of uniform compression. A pair of lines in the figure is associated with each value of μ. The upper line of the pair shows the ratio of the tangential to the normal component of the major principal stress, and the lower line shows the ratio of the components of the minor principal stress. If the majority of contacts were sliding, then by (7), the stress ratio would approach μ. This is not the case. The negative sign of the minor stress ratio shows that the normal and tangential components oppose each other, while the components of the major principal stress act together. The fact that the stress ratios approach zero in uniform compression does not mean that little sliding takes place, but rather means that the normal and tangential components become uncorrelated. The stress ratios were relatively insensitive to variations of F and h^*.

Nearly all of the energy lost during deformation is dissipated by ridge building and in-plane frictional sliding between ice parcels. The partition of the energy dissipation between the two processes is shown in Figure 15. The abscissa is the same as in Figure 14. The energy partition depends strongly on the friction coefficient μ between ice parcels. The results show that significant sliding occurs during uniform compression and that the two processes approach equipartition during pure shear. The energy partition was also found to depend on h^*. As was discussed above, decreasing h^* increases the constraints on deformation, forcing more sliding to occur. The energy partition was unaffected for $h^* = 1.5$ m (with $\mu = 0.5$) but approached the $\mu = 0.2$ curve in Figure 15 for $h^* = 1.25$ m (with $\mu = 0.5$). The energy partition was insensitive to variations of E.

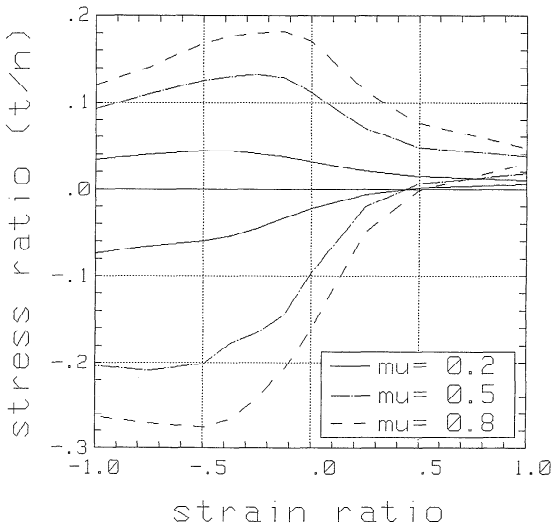

Figure 14. Ratio of the components of the (top) major and (bottom) minor principal stresses derived from the tangential and normal components of the contact forces between ice parcels for three values of the friction coefficient μ (using the 97% configurations).

Modeling Changes to the Ice Thickness Distribution Due to Pressure Ridging

The initial ice thickness distribution shown in Figure 7 is changed by the pressure ridging that accompanies deformation. At each ridge site, intact thin ice is destroyed to form ridge sails and keels. Less obviously, the ice rubble piled on and under intact floes and thin sheets indirectly destroys the area of the floe and sheet that is covered by moving it to thicker categories. The destruction of thin ice is determined by calculating the areas of overlap between ice parcels as shown in Figure 3. However, out-of-plane rubble piling is not explicitly modeled. Instead, the dimensions of the pressure ridges, implicitly created at each area of overlap between parcels as shown in Figures 3 and 4, are estimated from the results of ridging simulations [*Hopkins*, 1996]. The change in the area of ice in a given thickness range in the area surrounding a single ridge is shown in Figure 16, as a function of the volume of ice pushed into the ridge. The area and volume of ice are per meter of ridge length (perpendicular to the page in Figure 4).

The bottom line in Figure 16 shows the area of thin ice ($h = 0.5 \pm 0.25$ m) indirectly destroyed by rubble piled beneath the sheet. This corresponds to the diagonally shaded area on the left side of the ridge profile in Figure 4. The lower of the 2-m lines shows the area of floe ice ($h = 2 \pm 0.25$ m)

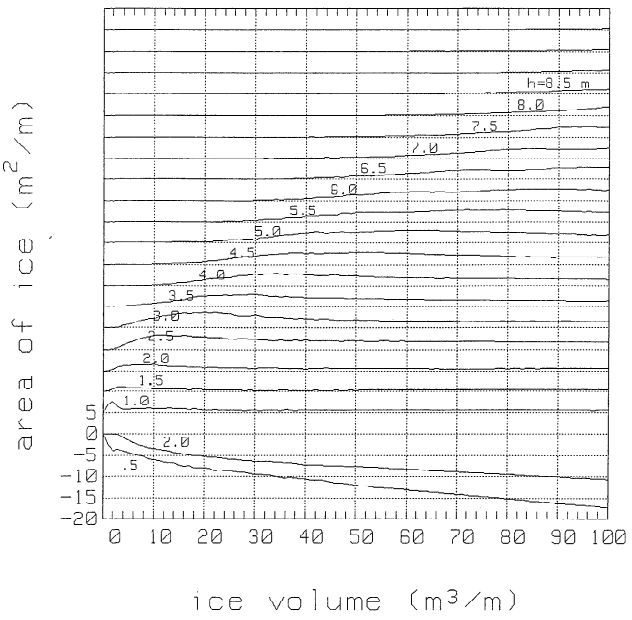

Figure 16. Change in the local ice thickness distribution in the area surrounding a single pressure ridge [*Hopkins*, 1996].

indirectly destroyed by rubble piled on and under the floe. This corresponds to the diagonally shaded area on the right side of the ridge profile in Figure 4. The lines above 0 are lines of creation. Each line is offset +5 m^2 from the previous line for clarity. For example, at a point where the volume of ridged ice is 20 m^3, about 3.5 m^2 of 3-m ice and 2 m^2 of 4-m ice have been created. The maximum thickness when the volume is 20 m^3 is 5 m. Note that 2-m ice is destroyed on the floe side and created on the lead side. Figure 16 does not include the area of thin ice that was converted into rubble that is calculated directly from the area of overlap between ice parcels. In order to use the data shown in Figure 16, the overlap area at a contact is divided into strips as shown in Figure 3. The volume of ridged ice in each strip hx is calculated, and the corresponding change in the area of ice in each thickness category is found from Figure 16. This process is repeated at each ridge site in the model pack.

The self-consistency of the procedure is compromised by the fact that Figure 16 applies to thin ice with thickness between 25 and 75 cm and thick ice with thickness between 1.75 and 2.25 m. About 60% of the contacts belong to this category. Contacts or ridge sites in which the thicknesses do not fall into these ranges are dealt with in the following manner. The functions in Figure 16 are split into two parts. One part corresponds to the area to the left of the floe edge and the other corresponds to the area to the right of the floe edge in Figure 4. Consider the area to the left of the floe edge. If the thin ice is thinner than 25 cm, then all the categories are moved down, so that the destruction line for 50-cm ice is used for ice in the range 0 to 25 cm. The creation line for 1-m ice is used for ice in the range 25 to 75 cm, and so on. If the thin ice is thicker than 75 cm, then all the categories are moved up. Thick ice less than 1.75 m thick is dealt with in a similar way. The accuracy of this approximation is reflected in the integration of (21) and (22) below.

The maximum sail heights of the ridges implicitly created in this manner follow the lognormal distribution shown in Figure 17. The data points give the cumulative distribution of sail heights. The results are from samples with area equal to 97% of the initial area. Sails less than 1 m in height were not considered. The mean sail height is 1.50 m, and the standard deviation is 0.56 m. There appeared to be no systematic relationship between sail height and the thickness of the parent (thin) ice sheet. *Sayed and Frederking* [1989], in measurements of first-year ridge sails in the southern Beaufort Sea, also found a lognormal distribution of sail heights and no correlation between sail height and ice thickness. However, *Tucker and Govoni* [1981], also in the Beaufort, found sail height to be approximately proportional to the square root of ice thickness.

If sail height is limited by the supply of thin ice (supply limited), then sail height is proportional to the square root of ridge volume or, equivalently, to the square root of the product of ice thickness and lead width. If ice thickness and lead width are uncorrelated, then sail height will be proportional to the square root of thickness [*Hibler*, 1980]. However, sail height may instead be limited by the available driving force (force limited). In this case, the ridge-building force is proportional to hV (equation (1)), where V is the volume of ridged ice. The sail height is proportional to the square root of the volume. Combining the two expressions to eliminate V leaves sail height proportional to the square root of force divided by thickness. Thus if sail height is limited by the available driving forces, then it should be inversely proportional to the square root of the ice thickness. In an area of the pack where some ridge sails may be force limited and others supply limited, the relationship between sail height and ice thickness will tend to disappear.

Ice Thickness Redistribution

Sophisticated ice-ocean models [*Hibler*, 1980; *Flato and Hibler*, 1995] are based on the ice thickness distribution theory developed by *Thorndike et al.* [1975]. The movement of ice from one thickness category to another thickness category of

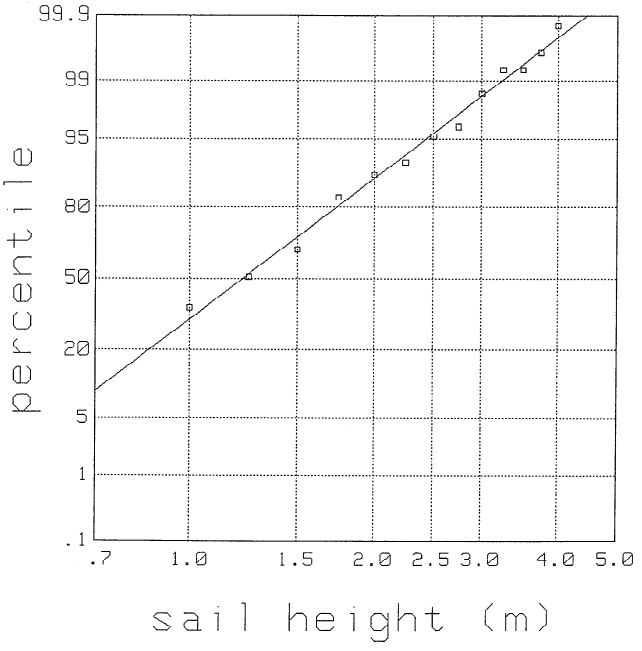

Figure 17. Lognormal plot of sail heights (using the 97% configurations). Only sails greater than or equal to 1 m in height are considered.

the thickness distribution is modeled by an assumed ice thickness redistribution function. The physical mechanisms behind the redistribution of ice are ridging, which mechanically thickens the ice, and opening, which creates leads. The redistribution function defined by Thorndike et al. is

$$\psi(h) = (e_I^2 + e_{II}^2)^{1/2}\{\alpha_0(\theta)w_0(h) + \alpha_r(\theta)w_r(h)\} \quad (20)$$

where $w_0(h = 0) \propto \delta(h)$ and $w_r(h)$ are called the opening and ridging modes. The coefficients α_0 and α_r depend on $\theta = \tan^{-1}(e_{II}/e_I)$, defined in terms of the strain rate invariants e_I and e_{II}. The expression $(e_I^2 + e_{II}^2)^{1/2}$, upon substitution of the principal stresses, is equal to (19).

The ridging mode $w_r(h)$ is composed of two parts. They are $a(h)$, the distribution of the ice participating in ridging (i.e., thin ice converted into rubble), and $n(h)$, the distribution of ice created by ridging. The distributions of ice created and destroyed in the model pack under various deformation fields are shown in Figure 18. Open water production, which is part of w_0, is not shown in Figure 18. The negative lines show the destruction of ice of a given thickness, while the positive lines show creation. The functions are normalized by the magnitude of the strain rate invariant (19).

The ridging mode $w_r(h)$, the sum of the functions $a(h)$ and $n(h)$, is shown in Figure 19 for various deformation states. The opening function $w_0(h = 0) \propto \delta(h)$ for the same deformation states is shown in the small window. (No attempt is made here to extract the coefficients α_0 and α_r from the functions w_0 and w_r shown in Figure 19.) The sum of w_0 and w_r is the ice thickness redistribution function ψ (equation (20)) divided by the strain rate invariant.

Thorndike et al. [1975] imposed two constraints on the redistribution function. The first,

$$\int \psi(h)\, dh = \text{div } \mathbf{v} \quad (21)$$

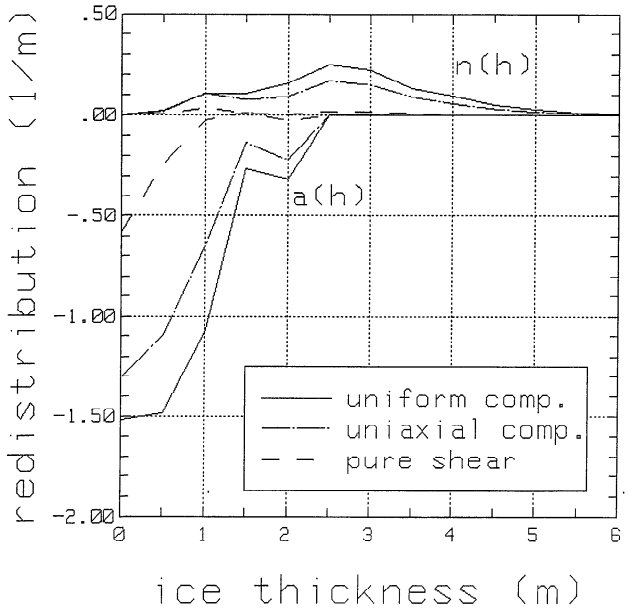

Figure 18. Ridging mode $w_r(h)$ from experiments using the 97% configurations. The creation ($n(h)$) and destruction ($a(h)$) parts of the ridging mode are normalized by the magnitude of the strain rate invariant (equation (19)).

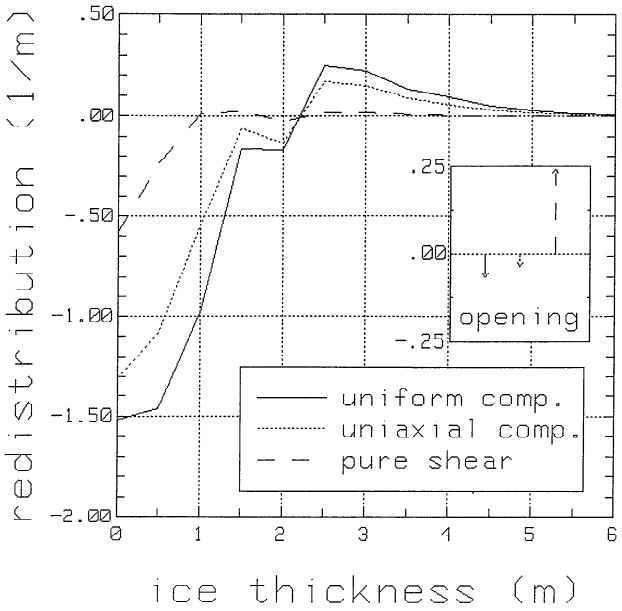

Figure 19. Ridging (w_r) and opening (w_0) parts of the ice thickness redistribution function from experiments using the 97% configurations. The functions are normalized by the magnitude of the strain rate invariant (equation (19)).

requires the redistribution function ψ to compensate for changes in area due to divergence. The second,

$$\int h\psi(h)\, dh = 0 \quad (22)$$

follows from the assumption that ridging does not alter the total volume of ice. The constraints provide a check on the self-consistency of the redistribution model described above. Multiplying the sum of $n(h)$ and $a(h)$ in Figure 19 by the strain rate invariant (equation (19)) and integrating gives the rate of change of area under the various deformation states. The rate of change of area differs from the divergence rate by less than 0.1% in all cases. Similarly, multiplying the separate functions $n(h)$ and $a(h)$ in Figure 18 by the strain rate invariant and thickness and integrating gives the volumetric rates of creation and destruction under the various deformation states. The difference between the two divided by their sum ranges from 1% in pure convergence to 6% in pure shear. A ridge porosity of 12%, calculated directly from the ridge profiles used in compiling Figure 16, was used in this calculation. This value, which sounds low by three-dimensional standards, is reasonable for a two-dimensional system, especially as it includes the presence of the solid floe.

Concluding Remarks

The mesoscale (10–100 km) computer model of the central Arctic ice pack is based on two key assumptions. The first is the assumption of a critical ice thickness h^* that separates and delimits two modes of plastic failure in the interactions between neighboring ice parcels. One, ridging of thin ice ($h < h^*$) caps elastic forces at low levels and the other, crushing of thick ice ($h > h^*$) caps elastic forces at very high levels. The very high cap on the elastic forces in crushing contacts permits only very small deformations between thick ice parcels at the

relatively low stress levels in the experiments. In the ice thickness distribution used in the numerical experiments, the thick ice occupies about 80% of the model domain. The high strength and concentration of the thick ice imposes geometric constraints on deformation which make a significant fraction of the remaining thin ice inaccessible. The geometric constraints overwhelm the effects of small changes in the ice thickness distribution on the stress/strain behavior of the model pack. The extent to which the geometric constraints are realistic depends to a large extent on the second assumption, namely, the random orientation of leads and spatial distribution of ice thicknesses. The patterns of thin ice filling the leads in the initial configuration of the model ice pack were not dynamically created. In contrast, deformation of a real ice pack may create well-defined lead systems. As the lead system freezes, it may result in a contiguous band of thin ice crossing a region of the pack. To the extent that subsequent convergence takes place perpendicular to these leads, the convergence will be geometrically unconstrained, and the nature of the rest of the surrounding pack will play no part in determining stress levels.

Stresses measured in numerical experiments with the model ice pack define yield curves in principal stress space. The results show the sensitivity of the magnitude of the yield curve to prior compressive deformation. Compressive deformation changes the model pack in three ways: by changing the ice thickness distribution, by increasing the amount of ridged ice at each ridging site, and by increasing the geometric constraints on deformation. Changes in the ice thickness distribution had little effect on the magnitude of the yield curves. However, the amount of ridged ice at each ridging site and the geometric constraints on deformation had a large effect on the magnitude of the yield curves. The shape of the yield curves suggests that the elliptical curve, used in large-scale modeling, represents the plastic behavior of the ice pack reasonably well. However, the strain rate vectors associated with points on the yield curves violate the normal flow rule. Use of the normal flow rule could lead to significant errors in estimating the associated state of stress. The magnitude and shape of the yield curves were found to be relatively unaffected by variations in the elastic modulus of the thin ice. However, the yield curves were sensitive to the critical thickness h^* and the coefficient of friction between ice parcels.

The results, for the first time, separate the effects of in-plane sliding between ice parcels and ridge building on the energy budget and the stress tensor. Not surprisingly, the partition of energy dissipation and the ratio of the stress components (caused by ridging and sliding) strongly depend on the coefficient of friction between ice parcels. Interestingly, the division of energy dissipation between ridging and sliding tends toward equipartition in pure shear, and sliding remains a significant energy sink even in uniform compression.

The redistribution functions calculated from the results of experiments with the ice pack model apply to a single thickness distribution. Systematic work with various distributions is needed to generalize the dependence of the redistributor and its components on the thickness distribution and the deformation state.

In its current form, the model is driven by a uniform mean strain field. The mean strain field could be replaced by wind drag, water drag, and deformable boundaries. Such an externally forced model could, in principle, be used in place of a single grid cell in a large-scale finite difference model of the Arctic Basin to produce detailed information about conditions around some point of interest, such as an offshore structure. However, in such a long-term simulation, some technique would be required to deal with the proliferation of detail created by a long series of deformations of the model domain. The proliferation would come from the creation of new thin ice parcels by thermodynamic growth in leads and the changing shape of existing, partially ridged thin ice parcels.

Acknowledgments. This work was supported by the NASA Polar Research Program (578-31-15-02) directed by Robert H. Thomas. The author would like to thank Greg Flato for his suggestions, which have improved the manuscript.

References

Cundall, P. A., and O. D. L. Strack, A discrete numerical model for granular assemblies, *Geotechnique*, *29*, 47–65, 1979.

Flato, G. M., and W. D. Hibler III, Ridging and strength in modeling the thickness distribution of Arctic sea ice, *J. Geophys. Res.*, *100*(C9), 18,611–18,626, 1995.

Fortune, S. J., A sweepline algorithm for Voronoi diagrams, *Algorithmica*, *2*, 153–174, 1987.

Hibler, W. D., III, A dynamic thermodynamic sea ice model, *J. Phys. Oceanogr.*, *9*, 815–846, 1979.

Hibler, W. D., III, Modeling a variable thickness sea ice cover, *Mon. Weather Rev.*, *108*, 1943–1973, 1980.

Hibler, W. D., III, Ice dynamics, in *The Geophysics of Sea Ice*, edited by N. Untersteiner, pp. 577–640, Plenum, New York, 1986.

Hopkins, M. A., The numerical simulation of systems of multitudinous polygonal blocks, *CRREL Rep.* 92-22, Cold Reg. Res. and Eng. Lab., U.S. Army Corps of Eng., Hanover, N. H., 1992.

Hopkins, M. A., A mesoscale simulation of the Arctic ice pack, in *Ice Mechanics—1993*, edited by J. P. Dempsey, Z. P. Bazant, Y. D. S. Rajapakse, and S. S. Sunder, pp. 85–96, Am. Soc. of Mech. Eng., New York, 1993.

Hopkins, M. A., On the ridging of an intact sheet of lead ice, *J. Geophys. Res.*, *99*(C8), 16,351–16,360, 1994.

Hopkins, M. A., The effects of individual ridging events on the ice thickness distribution in the Arctic ice pack, *Cold Reg. Sci. Technol.*, *24*, 75–82, 1996.

Hopkins, M. A., and W. D. Hibler III, Numerical simulations of a compact convergent system of ice floes, *Ann. of Glaciol.*, *15*, 26–30, 1991.

Mellor, M., Mechanical behavior of sea ice, in *The Geophysics of Sea Ice*, edited by N. Untersteiner, pp. 165–202, Plenum, New York, 1986.

Sayed, M., and R. M. W. Frederking, Measurements of ridge sails in the Beaufort Sea, *Can. J. Civ. Eng.*, *16*, 16–21, 1989.

Thorndike, A. S., D. A. Rothrock, G. A. Maykut, and R. Colony, The thickness distribution of sea ice, *J. Geophys. Res.*, *80*, 6565–6575, 1975.

Tucker, W. B., III, and J. W. Govoni, Morphological investigations of first-year sea ice pressure ridge sails, *Cold Reg. Sci. Technol.*, *5*, 1–12, 1981.

Wadhams, P., Sea-ice topography of the Arctic Ocean in the region 70W to 25E, *Philos. Trans. R. Soc. London*, *302*(1464), 45–85, 1981.

M. A. Hopkins, Cold Regions Research and Engineering Laboratory, U.S. Army Corps of Engineers, 72 Lyme Road, Hanover, NH 03755-1290. (e-mail: hopkins@hanover-crrel.army.mil)

(Received May 3, 1995; revised April 25, 1996;
accepted May 2, 1996.)